Applied Catalysis B: Environmental 184 (2016) 28–34

Contents lists available at ScienceDirect

Applied Catalysis B: Environmental

journal homepage: www.elsevier.com/locate/apcatb

Enhanced photocatalytic oxidation of NO over g-C_3N_4-TiO_2 under UV and visible light

Jinzhu Ma, Caixia Wang, Hong He*

State Key Joint Laboratory of Environment Simulation and Pollution Control, Research Center for Eco-Environmental Sciences, Chinese Academy of Sciences, Beijing 100085, China

ARTICLE INFO

Article history:
Received 22 September 2015
Received in revised form
12 November 2015
Accepted 14 November 2015
Available online 19 November 2015

Keywords:
TiO_2
Graphitic-C_3N_4
Photocatalysis
NO_x removal
Radical species

ABSTRACT

In this work, graphitic carbon nitride-titanium dioxide (g-C_3N_4-TiO_2) was successfully prepared by a facile calcination route utilizing commercial P25 and melamine as the precursors. The as-prepared g-C_3N_4/TiO_2 photocatalysts were characterized systematically to elucidate their morphological structure and physicochemical properties. The photocatalytic performance of g-C_3N_4-TiO_2 composites was investigated for the removal of NO_x in air. At the optimal g-C_3N_4 content (~15 wt%, labeled as M400), the conversion of NO_x was 27%, which is higher than that of pure P25 (17%) and g-C_3N_4 (7%) under visible light. The activity of M400 was also enhanced under UV light. However, a mechanically mixed g-C_3N_4 and TiO_2 sample (with the content of g-C_3N_4 the same as M400, labeled as M0 + g-C_3N_4) did not improve the conversion of NO_x. Therefore, the interaction of g-C_3N_4 and P25 is important for the activity. EPR results indicated that $^{\bullet}O_2^-$ is the main active species for NO oxidation to NO_3^- under visible and UV light, which is responsible for the difference in activity between M400 and M0 + g-C_3N_4. The present study can improve our understanding of NO removal on the photocatalyst surface and the mechanism for the activity enhancement by the formation of g-C_3N_4-TiO_2.

1. Introduction

Nitrogen oxides (NO_x), mainly derived from the combustion of fossil fuels, are responsible for environmental problems such as acid rain, photochemical smog, haze, and so on [1,2]. Over the past decades, the concentration of NO_x in the atmosphere has greatly increased because of the fast growth of energy consumption [1]. Selective catalytic reduction (SCR), wet scrubbing, adsorption, biofiltration, and catalytic decomposition, can remove NO_x from emission sources; however, they cannot be used for the removal of NO_x at parts per billion (ppb) levels in the air [3,4]. Semiconductor photocatalysis, as a "green" technology that utilizes sunlight to decomposition air pollutants at ambient conditions, has been used to remove low concentration NO_x [5–11].

Recently, graphitic carbon nitride (g-C_3N_4) has turned out to be a fascinating choice for a photocatalyst due to its high stability with respect to thermal (up to 600 °C in air) and chemical attacks (e.g., acid, base, and organic solvents) and an appealing electronic structure, having a medium band gap [12–14]. Graphitic-C_3N_4 has been used for the photocatalytic removal of NO in air [10,15–17]. Because of its small surface area and fast electron-hole recombination, the application of g-C_3N_4 is not ideal [18]. Mesoporous g-C_3N_4 with specific surface area of 200–500 m^2/g can provide more sites for the reaction; however, a template is often needed in the preparation, which is complicated [19–22]. A composite of g-C_3N_4 and metal oxide can improve the surface area of the photocatalyst and promote the separation of photogenerated electrons and holes, so as to improve the photocatalytic activity. Compared with the traditional TiO_2 photocatalyst, the conduction band electrons of g-C_3N_4 have stronger reduction ability, and can effectively activate molecular oxygen and produce more superoxide radicals for photocatalytic degradation of pollutants [12]. g-C_3N_4-TiO_2 composites have been widely investigated for the photocatalytic degradation of pollutants, and g-C_3N_4 modification was found to effectively enhance the activity of photocatalysts [23–35]. In all these studies, TiO_2 was prepared during the experimental processes, but there were a few reports about composites prepared with P25, the well-known popular commercial photocatalyst with the best photocatalytic activity under UV irradiation [36–38]. Importantly, the studies mostly investigated the effect on the visible light activity [36,38] and ignored the effect on the UV light activity, which is also important for the practical application of photocatalysts in the

* Corresponding author. Fax: +86 10 62849123.
E-mail address: honghe@rcees.ac.cn (H. He).

http://dx.doi.org/10.1016/j.apcatb.2015.11.013

outdoors. Additionally, to the best of our knowledge, the use of g-C_3N_4-TiO_2 materials for photocatalytic removal of NO_x has not been reported.

In this work, g-C_3N_4-TiO_2 was successfully prepared by a facile calcination route utilizing commercial P25 and melamine as the precursors. The as-prepared g-C_3N_4/TiO_2 photocatalysts were characterized by XRD, TGA, Raman, TEM, XPS, N_2 adsorption–desorption, UV–vis, PL and EPR. The photocatalytic performance was systematically evaluated for removal of NO_x under visible and UV light.

2. Experimental

2.1. Catalyst synthesis

The photocatalysts were synthesized by calcining mixtures of P25 and melamine. In a typical synthesis procedure, 1 g P25 was dispersed in 30 mL distilled water, and then a given amount of melamine was added. The mixed solution was uniformly agitated for 30 min, and then dried in air at 60 °C. Finally, the mixture was sealed in a crucible with a cover, which was then maintained at 550 °C in a muffle furnace (the heating ramp is 15 °C/min) for 4 h and the atmosphere for the heating process is air. The weight percentage ratio of melamine against P25 in the precursors was controlled to be 0, 65, 300, 330, 400, 500 and 600 wt%, and the resulting photocatalysts were labeled as M0 (P25), M65, M300, M330, M400, M500 and M600, respectively. The actual loading amounts of g-C_3N_4 on the M65, M300, M330, M400, M500 and M600 samples were estimated to be about 0.1, 0.58, 3.23, 15.06, 36.75 and 55.93 wt%, respectively (determined by TGA, See Fig. S1). Pure g-C_3N_4 was prepared (with the absence of P25) for comparison. A photocatalyst having the same content of g-C_3N_4 as M400 was prepared by mechanical mixing of the appropriate amount of M0 and pure g-C_3N_4, and labeled as M0 + g-C_3N_4. The amount of g-C_3N_4 in M0 + g-C_3N_4 was determined to be 15.62 wt% by TGA (data not shown).

2.2. Characterization

The crystalline structure of the samples were determined by a powder X-ray diffractometer (XRD; X'Pert PRO, PANalytical, Netherlands) using Cu $K\alpha$ (λ = 0.15406 nm) radiation. The data of 2θ from 20° to 80° were collected with the step size of 0.05°.

The contents of g-C_3N_4 of the as-prepared photocatalysts were characterized using thermal gravimetric analysis (TGA) with a TGA/DSC1 STAR^e system (METTLER TOLEDO). About 15 mg of each photocatalyst was heated up to 800 °C under 100 mL/min air flow at a heating rate of 10 °C/min.

Raman spectra of the photocatalysts were recorded on a home-made UV resonance Raman spectrometer (UVR DLPC-DL-03), which was calibrated against the Stokes Raman signal of Teflon at 1378 cm^{-1}. A 532 nm laser beam and a 325 nm He-Cd laser was used as an exciting source for the measurement of Raman.

Transmission electron microscopy (TEM) images were obtained using a JEOL JEM-2100 electron microscope (JEOL, Japan).

X-ray photoelectron spectroscopy (XPS) of the samples were recorded on a Scanning X-ray Microprobe (AXIS Ultra, Kratos Analytical, Inc.) using Al $K\alpha$ radiation. Binding energies were calibrated using the C 1s peak (BE = 284.8 eV) as standard.

The specific surface area of the photocatalysts were determined with a physisorption analyzer (Autosorb-1C-TCD, Quantachrome, USA) by N_2 adsorption-desorption at 77 K. Prior to the N_2 physisorption, all samples were degassed at 300 °C for 5 h.

The UV–vis diffuse reflection spectra were recorded in air with $BaSO_4$ as a reference with a diffuse reflectance UV–vis Spectrophotometer (U-3310, Hitachi).

The photoluminescence (PL) spectra of the photocatalysts were measured in a home-built laser-induced luminescence spectrograph. Prior to the experiments, the wavelength was calibrated with a mercury lamp. A 325 nm He-Cd laser was used as the exciting source.

The X-band electron paramagnetic resonance (EPR) spectra were recorded at room temperature using a Bruker A300-10/12 EPR spectrometer. The sample for EPR measurement was prepared by adding the photocatalysts to a 0.08 mol/L 5,5′-dimethyl-1-pirroline-*N*-oxide (DMPO) solution with aqueous dispersion for DMPO-$^{\bullet}OH$ and methanol dispersion for DMPO-$^{\bullet}O_2^-$. The photocatalysts was irradiated with the aforementioned visible light or UV light for 5 min. The EPR measurement was performed immediately after the illumination. Typical instrumental settings were as follows: microwave power 23.16 mW, microwave frequency 9.85 GHz, modulation frequency 100 kHz, modulation amplitude 3 G, time-constant 20.48 ms, sweep time 81.92 s.

2.3. Photocatalytic NO removal

The photocatalytic experiments for the removal of NO with the resulting samples were performed at ambient temperature in a continuous flow reactor, similar to our previous work [39,40] and are fully described in SI. Briefly, for the visible light photocatalytic activity test, a 500-W commercial Xenon arc lamp (Beijing TrusTech Science and Technology Co., China) with two optical filters were used to obtain light in the 420–700 nm range, and the integrated light intensity was 35.8 mW/cm^2. For the UV light photocatalytic activity test, a 500-W commercial Hg lamp (Beijing TrusTech Science and Technology Co., China) was used as the light source with an optical filter (λ = 365–366 nm), and the average light intensity was 84.7 mW/cm^2. 0.05 g photocatalysts was used for each experiment. The initial concentration of NO was 400 ppb and the relatively humidity of the gas was 55%. The total flow rate was controlled at 1.2 L min^{-1}. The concentration of NO, NO_2 and NO_x was measured by a chemiluminescence NO_x analyzer (Thermo Environmental Instruments Inc. Model 42i).

The NO conversion, NO_2 selectivity and NO_x conversion were defined as follows:

$$\text{NOconversion} = \frac{[NO]_{in} - [NO]_{out}}{[NO]_{in}}$$

$$NO_2\text{selectivity} = \frac{[NO_2]_{out}}{[NO]_{in} - [NO]_{out}}$$

$$NO_x \text{ conversion} = \frac{[NO]_{in} - [NO_x]_{out}}{[NO]_{in}}$$

3. Results and discussion

3.1. Photocatalytic NO removal activity

NO cannot be removal with or without light in the absence of photocatalyst (residence time 5.7 s). The NO conversion, NO_x conversion and NO_2 selectivity at 0.5 h for various photocatalysts under visible light are displayed in Fig. S2. It can be seen that the incorporation of g-C_3N_4 on P25 can improve the conversion of NO_x. The photocatalytic activity of the g-C_3N_4/P25 photocatalyst is highly dependent on the amount of g-C_3N_4. The conversion of NO_x on M400 was higher than that of other photocatalysts; this means that the optimum g-C_3N_4 content is ~15 wt%. Therefore, we chose M400

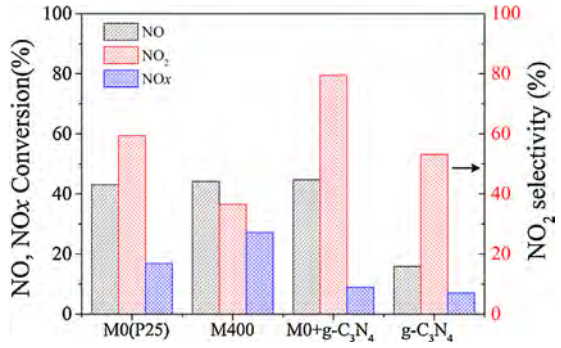

Fig. 1. The NO conversion, NO_x conversion and NO_2 selectivity at 0.5 h for M0, M400, M0 + g-C_3N_4 and g-C_3N_4 under visible light.

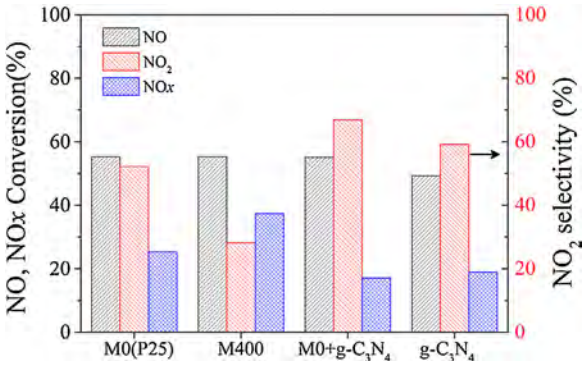

Fig. 2. The NO conversion, NO_x conversion and NO_2 selectivity at 0.5 h for M0, M400, M0 + g-C_3N_4 and g-C_3N_4 under UV light.

as the optimal content to carry out our further investigations. Fig. 1 shows the NO conversion, NO_x conversion and NO_2 selectivity at 0.5 h for M0, M400, M0 + g-C_3N_4 and g-C_3N_4 under visible light. As we can see, the conversion of NO was about 44% over M0, M400 and M0 + g-C_3N_4, however, the NO_2 selectivity (~36%) was lowest over M400, and therefore the conversion of NO_x (~27%) was highest over M400. The activity of M400 was higher than that the sum of M0 (17%) and g-C_3N_4 (7%). However, the photocatalysts prepared by mechanical mixing of g-C_3N_4 (the same content with M400) and M0 did not improve the conversion of NO_x (The conversion of NO was similar to that of M400, but the NO_2 selectivity for (~80%) was high.). Therefore, the interaction of g-C_3N_4 and P25 is important for the activity, which will be discussed in the following part.

Because of P25 is a well-known UV-response photocatalyst, the activity under UV light is also important for the practical application of the photocatalysts. Fig. 2 shows the NO conversion, NO_x conversion and NO_2 selectivity at 0.5 h for M0, M400, M0+g-C_3N_4 and g-C_3N_4 under UV light. Similar to the visible light activity, the UV light activity of M400 was enhanced, but the photocatalyst prepared by mechanical mixing of g-C_3N_4 (the same content as M400) and M0 did not improve the conversion of NO_x. These results further indicate that the interaction of g-C_3N_4 and P25 is important for the activity.

3.2. The crystal structure of the photocatalysts

XRD was used to determine the phase structures and average crystal size of the as-prepared photocatalysts. Fig. 3 illustrates the XRD patterns of photocatalysts prepared at different weight rations of g-C_3N_4 and TiO_2. It can be seen that the TiO_2 phases in pure P25 (M0) and the g-C_3N_4/P25 photocatalysts (M65, M175, M400, M500, M600 and M0 + g-C_3N_4) were anatase (JCPDS no. 21–1272) and rutile (JCPDS no. 21–1276), and the weight ratio of anatase was

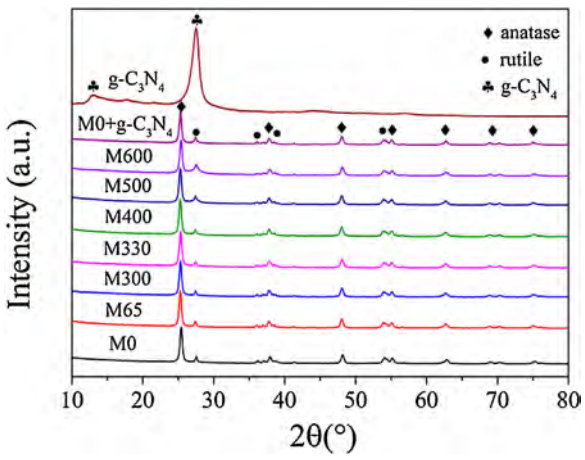

Fig. 3. XRD patterns of M0, M65, M300, M330, M400, M500, M600, M0 + g-C_3N_4 and pure g-C_3N_4.

about 80%. For pure g-C_3N_4, two main diffraction peaks at $2\theta = 27.5^\circ$ and 13.0° can be observed, which indicates the formation of g-C_3N_4 (JCPDS no. 87–1526). The stronger peak at 27.4° was the (002) diffraction peak and represents the interplanar graphitic stacking with an interlayer distance of 0.325 nm. The minor peak at around 13.0° corresponds to the (100) diffraction peak and represents an interplanar separation of 0.681 nm [10,41]. No obvious changes of the positions and intensities of the characteristic diffraction peaks of anatase and rutile were observed for any of the g-C_3N_4/P25 photocatalysts. This implies that the existence of g-C_3N_4 did not have a significant influence on the phase structure of TiO_2 in the as-prepared photocatalysts. The crystallite size of the photocatalyst was determined from the half-width of peaks by using Scherrer's formula ($d = 0.9\lambda/\beta \cos\theta$) on the basis of the anatase [101] and rutile [110] peaks. All g-C_3N_4/P25 photocatalysts have almost the same crystallite size (ca. 21 nm for anatase and 33 nm for rutile), indicating that the addition of g-C_3N_4 has no obvious influence on the crystallite size and morphology of TiO_2.

3.3. The interaction between g-C_3N_4 and TiO_2

Raman spectroscopy can be used to clearly characterize the surface structure of photocatalysts. Visible Raman spectra of M0, M400, M0 + g-C_3N_4 and g-C_3N_4 are displayed in Fig. S3. The presence of g-C_3N_4 results in a strong fluorescence on TiO_2. From the fluorescence signal intensity, it can be seen the content of g-C_3N_4 on the surface of M400 is higher than that on the surface of M0 + g-C_3N_4. UV Raman spectroscopy was found to be more sensitive to the surface region of TiO_2 than visible Raman spectroscopy and XRD because TiO_2 strongly absorbs UV light [42]. Fig. 4 illustrates the UV Raman spectra of M0, M400, M0 + g-C_3N_4 and g-C_3N_4. For g-C_3N_4, several characteristic peaks at 1624, 1576, 1481, 1258, 976, 759, 704, 582 and 474 cm^{-1} were observed, corresponding to the typical vibration modes of CN heterocycles [43,44]. The characteristic peaks of TiO_2 and weak characteristic peaks of g-C_3N_4 were observed on the surface of M400 and M0 + g-C_3N_4. The characteristic peaks of g-C_3N_4 were more pronounced on the surface of M400, which further reveals that the content of g-C_3N_4 on the surface of M400 is higher than that on the surface of M0 + g-C_3N_4. These results indicate that g-C_3N_4 is more evenly distributed on the surface of M400 than that on the surface of M0 + g-C_3N_4.

The morphology of the photocatalyst was examined by TEM. Fig. 5 shows the TEM micrographs of M0, M400, M0 + g-C_3N_4 and g-C_3N_4. It can be seen that pure TiO_2 (Fig. 5a) shows spherical particles whereas pure g-C_3N_4 (Fig. 5d) displays a 2D lamellar structure. For M400 (Fig. 5b), the TiO_2 nanoparticles are embedded in the g-C_3N_4

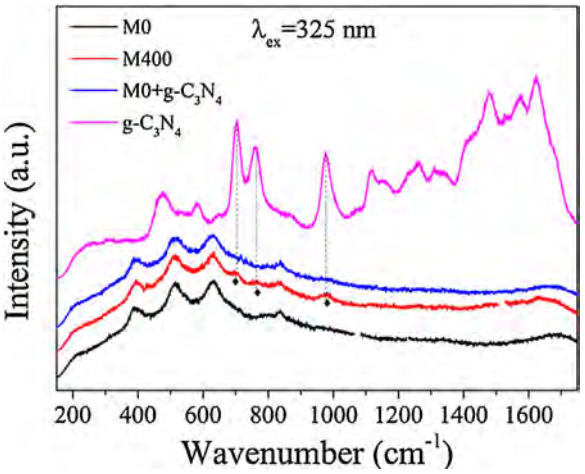

Fig. 4. UV Raman spectroscopy of M0, M400, M0 + g-C_3N_4 and g-C_3N_4.

lamellar structure. For the M0 + g-C_3N_4 sample (Fig. 5c), parts of the TiO_2 nanoparticles are embedded in the g-C_3N_4 lamellar structure. These observations were consistent with the Raman results, further indicating that g-C_3N_4 is more evenly distributed on the surface of M400 than on the surface of M0 + g-C_3N_4. These observations suggest the formation of a heterojunction between TiO_2 and g-C_3N_4, which would be an ideal system to achieve improved electron-hole separation [37].

More detailed information regarding the chemical composition of the as-prepared photocatalysts and the chemical status of the Ti, C and N elements in the photocatalyst was obtained using X-ray photoelectron spectroscopy. The survey spectrum of M0, M400, M0 + g-C_3N_4 and g-C_3N_4 is shown in Fig. S4. The g-C_3N_4 sample exhibited C1s and N1s signals with a C/N molar ratio of 0.75 (Table S1), in agreement with the ideal C_3N_4 composition (C/N = 0.75). As shown in Table S1, More N atoms and less O and Ti atoms were observed for M400 than that for M0 + g-C_3N_4, which indicates that g-C_3N_4 is more uniformly dispersed on the surface of M400, consistent with the Raman and TEM results.

The BET specific surface areas of the M0, M400, M0 + g-C_3N_4 and g-C_3N_4 samples were 41.9 m^2/g, 60.8 m^2/g, 53.4 m^2/g and 18.0 m^2/g, respectively. The increase of the BET specific surface areas of M400 may be due to that TiO_2 nanoparticles embedded in the g-C_3N_4 lamellar structure leads to the formation of thinner lamellar g-C_3N_4 for g-C_3N_4-TiO_2. For M0 + g-C_3N_4, the grinding may leads to the exfoliation of g-C_3N_4, which increases the BET surface areas of the photocatalysts. This needs to be studied further. However, this is not the focus of this study. The BET specific surface area of M400 and M0 + g-C_3N_4 was similar but the activity was different, indicating the surface area is not the key factor for the improvement of the activity.

3.4. UV–vis diffuse reflectance spectra and band structure

Fig. 6a shows the UV–vis diffuse reflectance spectra (DRS) of the synthesized photocatalysts. The band gap values of the synthe-

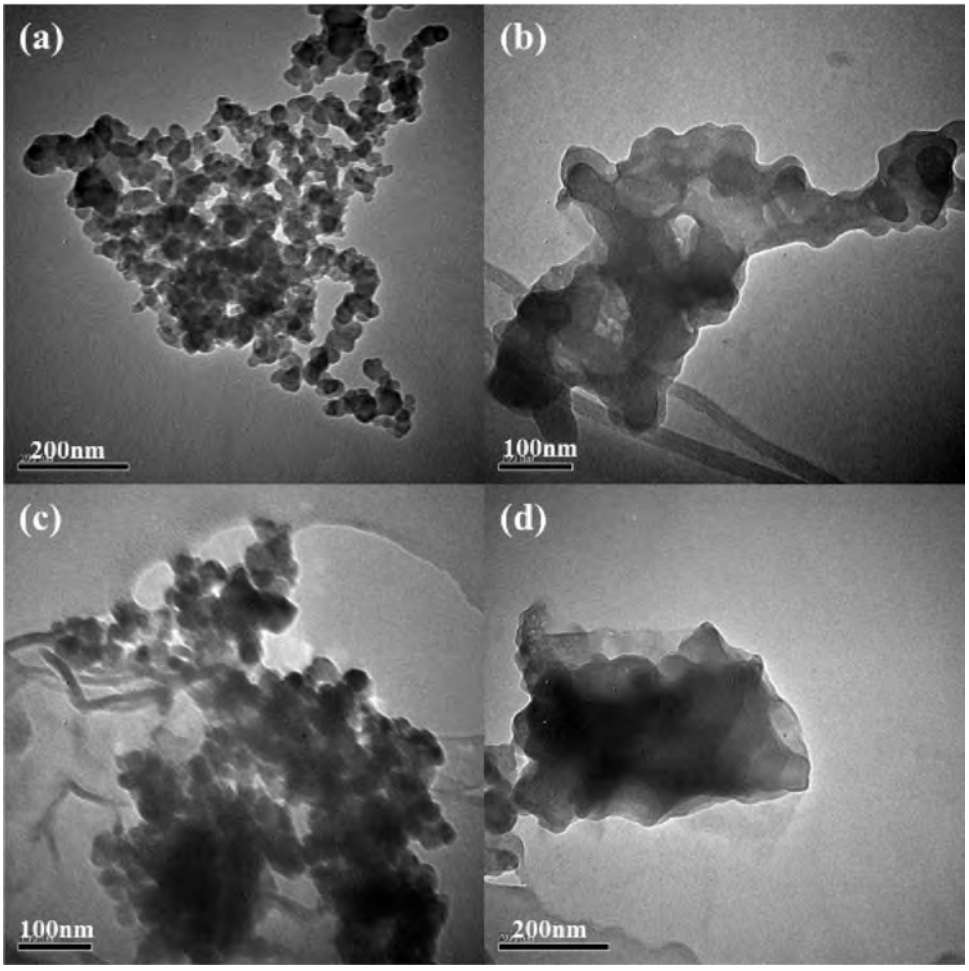

Fig. 5. TEM images of (a) M0, (b) M400, (c) M0 + g-C_3N_4 and (d) g-C_3N_4.

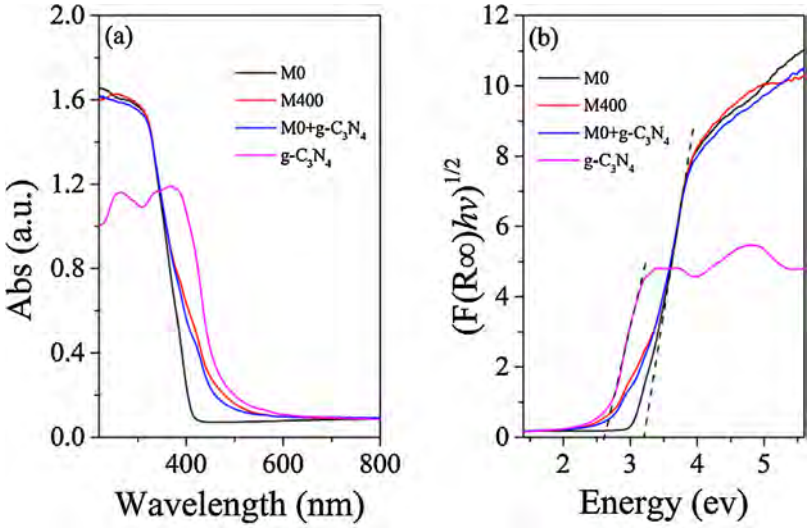

Fig. 6. (a) UV–vis diffuse reflectance spectra and (b) plots of transformed Kubelka–Munk function versus the energy of absorbed light for the M0, M400, M0 + g-C_3N_4 and g-C_3N_4.

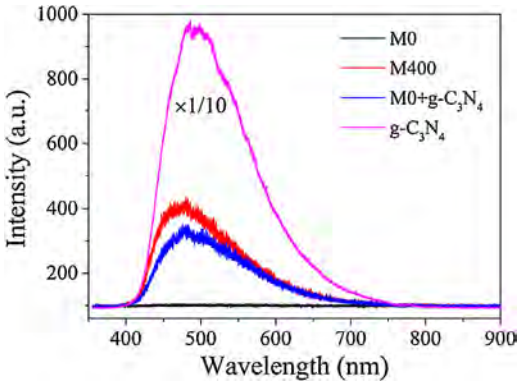

Fig. 7. The photoluminescence (PL) emission spectra of the M0, M400, M0 + g-C_3N_4 and g-C_3N_4.

sized photocatalysts were calculated by plots of $(F(R_\infty)h\nu)^{1/2}$ versus photo energy, as shown in Fig. 6b. The absorption onset of g-C_3N_4 is at about 475 nm, corresponding to a band gap energy of 2.6 eV. This is consistent with previous work [12]. The band gap of M0 is about 3.2 eV, with an absorption edge of 384 nm. After hybridization with g-C_3N_4, the absorbance of M400 and M0 + g-C_3N_4 is extended to the visible region due to the presence of g-C_3N_4. Compared to M0, no significant shift of the absorption edge occurs, indicating similar band gap energies. This composite photocatalyst can improve the utilization of the visible light.

3.5. Photoluminescence emission spectra

PL emission spectra of the photocatalysts are shown in Fig. 7, revealing that the peaks are nearly identical in shape and position for all of the photocatalysts. The PL intensity of M400 and M0 + g-C_3N_4 was significantly reduced in comparison with pure g-C_3N_4, indicating that the electron-hole recombination on the surface of these photocatalysts was largely inhibited, to generate more photoelectrons and holes to participate in the photocatalytic reaction. This may be because the heterojunction formed at the interface between g-C_3N_4 and P25 can prevent the recombination of photo-generated charge effectively. The PL intensity of M0 is low, probably because the amount of photogenerated electron-hole pairs is lower under the same irradiation conditions. Similar results were observed on the red phosphorus/g-C_3N_4 and BiOBr/g-C_3N_4 heterojunction systems by other groups [15,45].

3.6. Electron paramagnetic resonance spectra

To understand the performance difference between M400 and M0 + g-C_3N_4, DMPO spin-trapping EPR measurements were employed in methanol dispersion for DMPO-$^\bullet O_2^-$ and aqueous dispersion for DMPO-$^\bullet$OH. The characteristic peaks of both $^\bullet O_2^-$ and $^\bullet$OH radicals can be observed under visible light and UV light illumination (Fig. 8). The signal of $^\bullet O_2^-$ is much stronger than that of $^\bullet$OH under visible light. This is because visible light can only excite g-C_3N_4, and the valence band (VB) holes (~1.40 eV) from g-C_3N_4 cannot directly oxidize OH^- or H_2O into $^\bullet$OH radicals (1.99 eV for OH^- /$^\bullet$OH and 2.37 eV for H_2O/$^\bullet$OH). The $^\bullet$OH radicals should be generated via the $^\bullet O_2^- \rightarrow H_2O_2 \rightarrow {}^\bullet$OH route. These results confirm that $^\bullet O_2^-$ is the main active species, and $^\bullet$OH plays a minor role in NO_x oxidation under visible light. In addition, the VB holes of g-C_3N_4 might also oxidize NO because the $E_{\phi VB}$ (~1.4 eV versus normal hydrogen electrode (NHE)) of g-C_3N_4 is more positive than $E\phi(NO_2/NO)$, 1.03 eV versus NHE), $E_\phi(HNO_2/NO)$, 0.99 eV versus NHE), and E_ϕ (HNO_3/NO, 0.94 eV vs NHE) [10]. As shown in Fig. 1, the conversion of NO was similar over M400 and M0 + g-C_3N_4; however, the NO_2 selectivity over M400 was lower than that over M0+g-C_3N_4, and therefore the NO_x conversion was higher over M400. These results indicated that $^\bullet O_2^-$ is the main active species for the NO oxidation to NO_3^- under visible light.

The signal of $^\bullet O_2^-$ is similar to that of $^\bullet$OH under UV light. This is because UV light can excite both TiO_2 and g-C_3N_4. The VB holes (~2.85 eV) from TiO_2 can directly oxidize OH^- or H_2O into $^\bullet$OH radicals (1.99 eV for OH^-/$^\bullet$OH and 2.37 eV for H_2O/$^\bullet$OH), and the conduction bands (CB) from both TiO_2 (~−0.35 eV) and g-C_3N_4 (~−1.39 eV) can directly reduce the O_2 to $^\bullet O_2^-$ radicals (−0.33 eV for $O_2/^\bullet O_2^-$). These results confirm that $^\bullet O_2^-$, $^\bullet$OH and VB holes play a role in NO_x oxidation under UV light. As shown in Fig. 8, the signal of $^\bullet O_2^-$ is higher than that of $^\bullet$OH over M400, and the signal of $^\bullet O_2^-$ is lower than that of $^\bullet$OH over M0 + g-C_3N_4. Combined with the activity data in Fig. 2, this indicated that $^\bullet O_2^-$ is the main active species for the NO oxidation to NO_3^- under UV light.

On the basis of the above results and discussion, the photocatalytic mechanism for the M400 and M0 + g-C_3N_4 is tentatively

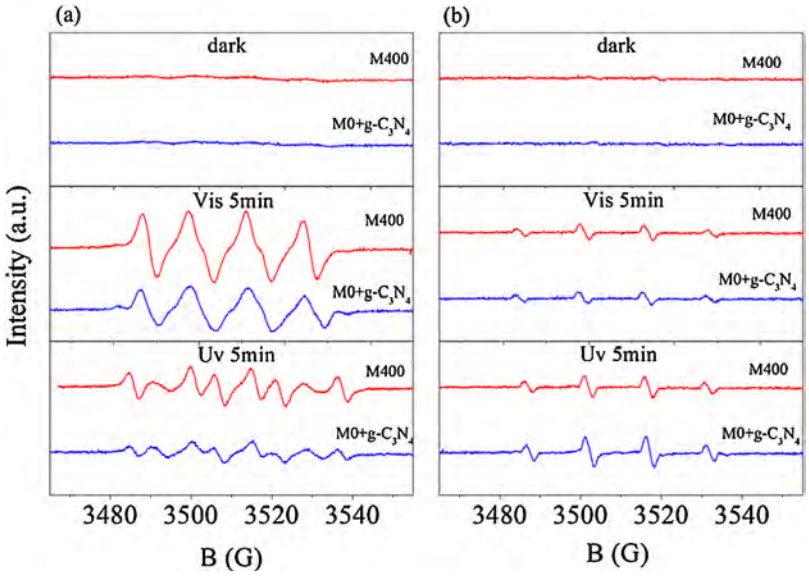

Fig. 8. DMPO spin-trapping EPR spectra of M400 and M0 + g-C_3N_4 (a) methanol dispersion for DMPO-•O_2^- and (b) aqueous dispersion for DMPO-•OH.

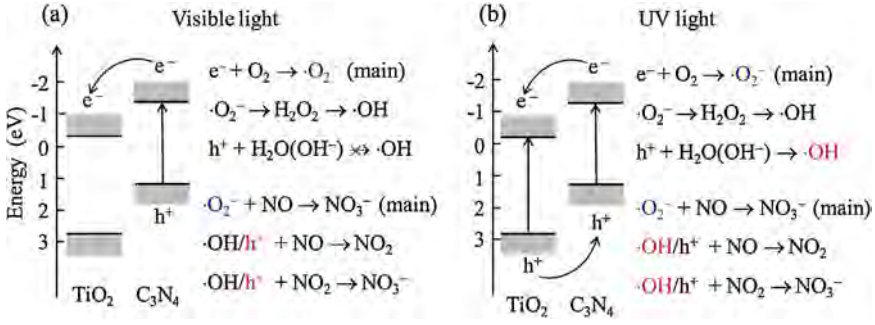

Fig. 9. Schematic illustration of the charge transfer, radical generation and NO oxidation on g-C_3N_4-TiO_2 under visible and UV light irradiation.

proposed and schematically illustrated in Fig. 9. Under visible light irradiation, g-C_3N_4 can be excited to induce the formation of photo-generated electrons and holes. The electrons could then migrate from the CB of g-C_3N_4 to the CB of TiO_2 via their interfacial interaction (Fig. 9a). Because interfacial interaction of M400 is better than that of M0 + g-C_3N_4, more electrons in g-C_3N_4 (CB) could easily transfer to TiO_2 (CB) in M400, and then more •O_2^- radical is generated, which is responsible for the NO oxidation to NO_3^- under visible light. Under UV light irradiation, both TiO_2 and g-C_3N_4 can be excited to induce the formation of photo-generated electrons and holes (Fig. 9b). The electrons in g-C_3N_4 (CB) could easily transfer to TiO_2 (CB), and the holes in TiO_2 (VB) could also easily transfer to g-C_3N_4 (VB) through their interfacial interaction. As a result, the recombination of the photo-generated electrons and holes is suppressed [46]. Because the interfacial interaction of M400 is better than that of M0 + g-C_3N_4, more electrons and holes were transferred; the holes transferred to g-C_3N_4 cannot directly oxidize OH^- or H_2O into •OH radicals, leading to more •O_2^- radical and less •OH on M400 (Fig. 8).

4. Conclusions

In summary, g-C_3N_4-TiO_2 composite photocatalysts were successfully prepared via a simple one-step calcination method utilizing commercial P25 and melamine as the precursors. Characterization results confirmed the formation of g-C_3N_4-TiO_2 composite photocatalysts, in which the TiO_2 nanoparticles are embedded in the g-C_3N_4 lamellar structure. The introduced g-C_3N_4 shows a great influence on the photocatalytic activity of the TiO_2. At the optimal g-C_3N_4 content (~15 wt%), the conversion of NO_x was enhanced under visible light and UV light. The conversion of NO_x on M0 + g-C_3N_4, which was prepared by the mechanical mixing of g-C_3N_4 and TiO_2 (the content of g-C_3N_4 is the same as for M400), was lower than that on M400. Therefore, the interaction of g-C_3N_4 and P25 is critical for the activity. Raman, TEM and XPS results indicate that g-C_3N_4 is more uniformly dispersed on the surface of M400 than on M0 + g-C_3N_4. The electron-hole recombination on the surface of M400 and M0 + g-C_3N_4 was significantly reduced in comparison with pure g-C_3N_4. EPR results indicated that •O_2^- is the main active species for the NO oxidation to NO_3^- under visible and UV light. Because the interfacial interaction of M400 is better than that of M0 + g-C_3N_4, more electrons in g-C_3N_4 (CB) could easily transfer to TiO_2 (CB) in M400, so that more •O_2^- radical is generated under visible light; on the other hand, more electrons and holes were transferred under UV light, and the hole transfer to g-C_3N_4 cannot directly oxidize OH^- or H_2O into •OH radicals, leading to more •O_2^- radical and less •OH on M400. These phenomena are responsible for the difference in activity between M400 and M0 + g-C_3N_4 for the oxidation of NO to NO_3^-. The present study can improve our understanding of NO removal on the photocata-

lyst surface and the mechanism for the enhancement of activity by the formation of g-C_3N_4-TiO_2.

Acknowledgments

This work was supported by the National Natural Science Foundation of China, (21207145) and the Strategic Priority Research Program of the Chinese Academy of Sciences, (XDB05050600). This work was also supported by the National Natural Science Foundation of China, (51221892).

Appendix A. Supplementary data

Supplementary data associated with this article can be found, in the online version, at http://dx.doi.org/10.1016/j.apcatb.2015.11.013.

References

[1] B. Zhao, S.X. Wang, H. Liu, J.Y. Xu, K. Fu, Z. Klimont, J.M. Hao, K.B. He, J. Cofala, M. Amann, Atmos. Chem. Phys. 13 (2013) 9869–9897.
[2] H. He, Y.S. Wang, Q.X. Ma, J.Z. Ma, B.W. Chu, D.S. Ji, G.Q. Tang, C. Liu, H.X. Zhang, J.M. Hao, Sci. Rep. 4 (2014) 4172, DOI:10.1038/srep04172.
[3] Z.H. Ai, W.K. Ho, S.C. Lee, J. Phys. Chem. C 115 (2011) 25330–25337.
[4] F. Dong, Y.J. Sun, M. Fu, W.-K. Ho, S.C. Lee, Z.B. Wu, Langmuir 28 (2012) 766–773.
[5] H. Yamashita, K. Yoshizawa, M. Ariyuki, S. Higashimoto, M. Che, M. Anpo, Chem. Commun. (2001) 435–436.
[6] J.L. Zhang, T. Ayusawa, M. Minagawa, K. Kinugawa, H. Yamashita, M. Matsuoka, M. Anpo, J. Catal. 198 (2001) 1–8.
[7] J.L. Zhang, Y. Hu, M. Matsuoka, H. Yamashita, M. Minagawa, H. Hidaka, M. Anpo, J. Phys. Chem. B 105 (2001) 8395–8398.
[8] F. Dong, Y. Huang, S.C. Zou, J.A. Liu, S.C. Lee, J. Phys. Chem. C 115 (2011) 241–247.
[9] G.H. Dong, W.K. Ho, L.Z. Zhang, Appl. Catal. B 168–169 (2015) 490–496.
[10] F. Dong, Z.Y. Wang, Y.H. Li, W.-K. Ho, S.C. Lee, Environ. Sci. Technol. 48 (2014) 10345–10353.
[11] F. Dong, Q.Y. Li, Y.J. Sun, W.-K. Ho, ACS Catal. 4 (2014) 4341–4350.
[12] X.C. Wang, S. Blechert, M. Antonietti, ACS Catal. 2 (2012) 1596–1606.
[13] Y.H. Zhang, Q.W. Pan, G.Q. Chai, M.R. Liang, G.P. Dong, Q.Y. Zhang, J.R. Qiu, Sci. Rep. 3 (2013) 1943, http://dx.doi.org/10.1038/srep01943.
[14] J. Liu, Y. Liu, N.Y. Liu, Y.Z. Han, X. Zhang, H. Huang, Y. Lifshitz, S.-T. Lee, J. Zhong, Z.H. Kang, Science 347 (2015) 970–974.
[15] Y.J. Sun, W.D. Zhang, T. Xiong, Z.W. Zhao, F. Dong, R.Q. Wang, W.-K. Ho, J. Colloid Interface Sci. 418 (2014) 317–323.
[16] T. Sano, S. Tsutsui, K. Koike, T. Hirakawa, Y. Teramoto, N. Negishi, K. Takeuchi, J. Mater. Chem. A 1 (2013) 6489–6496.
[17] F. Dong, Z.W. Zhao, T. Xiong, Z.L. Ni, W.D. Zhang, Y.J. Sun, W.-K. Ho, ACS Appl. Mater. Interfaces 5 (2013) 11392–11401.
[18] J.S. Zhang, J.H. Sun, K. Maeda, K. Domen, P. Liu, M. Antonietti, X.Z. Fu, X.C. Wang, Energy Environ. Sci. 4 (2011) 675–678.
[19] F. Goettmann, A. Fischer, M. Antonietti, A. Thomas, Angew. Chem. Int. Ed. 45 (2006) 4467–4471.
[20] M. Groenewolt, M. Antonietti, Adv. Mater. 17 (2005) 1789–1792.
[21] S.C. Lee, H.O. Lintang, L. Yuliati, Chem. -Asian J. 7 (2012) 2139–2144.
[22] X.C. Wang, K. Maeda, X.F. Chen, K. Takanabe, K. Domen, Y.D. Hou, X.Z. Fu, M. Antonietti, J. Am. Chem. Soc. 131 (2009) 1680–1681.
[23] K. Dai, L.H. Lu, C.H. Liang, Q. Liu, G.P. Zhu, Appl. Catal. B 156 (2014) 331–340.
[24] J.Y. Lei, Y. Chen, L.Z. Wang, Y.D. Liu, J.L. Zhang, J. Mater. Sci. 50 (2015) 3467–3476.
[25] X.F. Lu, Q.L. Wang, D.L. Cui, J. Mater. Sci. Technol. 26 (2010) 925–930.
[26] K. Sridharan, E. Jang, T.J. Park, Appl. Catal. B 142 (2013) 718–728.
[27] Z.A. Huang, Q. Sun, K.L. Lv, Z.H. Zhang, M. Li, B. Li, Appl. Catal. B 164 (2015) 420–427.
[28] X.-X. Zou, G.-D. Li, Y.-N. Wang, J. Zhao, C. Yan, M.-Y. Guo, L. Li, J.-S. Chen, Chem. Commun. 47 (2011) 1066–1068.
[29] J.W. Zhou, M. Zhang, Y.F. Zhu, Phys. Chem. Chem. Phys. 17 (2015) 3647–3652.
[30] L.A. Gu, J.Y. Wang, Z.J. Zou, X.J. Han, J. Hazard. Mater. 268 (2014) 216–223.
[31] X.S. Zhou, F. Peng, H.J. Wang, H. Yu, Y.P. Fang, Chem. Commun. 47 (2011) 10323–10325.
[32] M. Fu, J.M. Pi, F. Dong, Q.Y. Duan, H. Guo, Int. J. Photoenergy (2013) 158496.
[33] J.C. Shen, H. Yang, Q.H. Shen, Y. Feng, Q.F. Cai, CrystEngComm 16 (2014) 1868–1872.
[34] M.J. Munoz-Batista, A. Kubacka, M. Fernandez-Garcia, Catal. Sci. Technol. 4 (2014) 2006–2015.
[35] G.Y. Li, X. Nie, Y.P. Gao, T.C. An, Appl. Catal. B 180 (2016) 726–732.
[36] H.Q. Wang, J.Z. Li, C.C. Ma, Q.F. Guan, Z.Y. Lu, P.W. Huo, Y.S. Yan, Appl. Surf. Sci. 329 (2015) 17–22.
[37] J.G. Yu, S. Wang, J.X. Low, W. Xiao, Phys. Chem. Chem. Phys. 15 (2013) 16883–16890.
[38] H.L. Zhu, D.M. Chen, D. Yue, Z.H. Wang, H. Ding, J. Nanopart. Res. 16 (2014) 1–10.
[39] J.Z. Ma, H.M. Wu, Y.C. Liu, H. He, J. Phys. Chem. C 118 (2014) 7434–7441.
[40] J.Z. Ma, H. He, F.D. Liu, Appl. Catal. B 179 (2015) 21–28.
[41] F. Dong, Y.J. Sun, L.W. Wu, M. Fu, Z.B. Wu, Catal. Sci. Technol. 2 (2012) 1332–1335.
[42] J. Zhang, M.J. Li, Z.C. Feng, J. Chen, C. Li, J. Phys. Chem. B 110 (2006) 927–935.
[43] Q.J. Xiang, J.G. Yu, M. Jaroniec, J. Phys. Chem. C 115 (2011) 7355–7363.
[44] J.Z. Jiang, O.Y. Lei, L.H. Zhu, A.M. Zheng, J. Zou, X.F. Yi, H.Q. Tang, Carbon 80 (2014) 213–221.
[45] Y.-P. Yuan, S.-W. Cao, Y.-S. Liao, L.-S. Yin, C. Xue, Appl. Catal. B 140 (2013) 164–168.
[46] G.Y. Li, X. Nie, J.Y. Chen, Q. Jiang, T.C. An, P.K. Wong, H.M. Zhang, H.J. Zhao, H. Yamashita, Water Res. (2016), http://dx.doi.org/10.1016/j.watres.2015.1005.1053 (in press).